# Local symmetry breaking and magnetic properties of acceptor-donor codoped $Ca_3Mn_2O_7$ hybrid improper ferroelectrics

Yu Zhao,[1,2,*] Wenyue Zhao,[1,*] Weili Li,[1,3] Ze Li,[1] Zhao Wang,[1] Yazhou Peng,[1] Lidong Wang,[1,†] and Wei-Dong Fei[1,4,‡]

[1]*School of Materials Science and Engineering, Harbin Institute of Technology, Harbin 150001, People's Republic of China*

[2]*Laboratory for Space Environment and Physical Sciences, Harbin Institute of Technology, Harbin 150001, People's Republic of China*

[3]*National Key Laboratory of Science and Technology on Precision Heat Processing of Metals, Harbin Institute of Technology, Harbin 150001, People's Republic of China*

[4]*State Key Laboratory of Advanced Welding and Joining, Harbin Institute of Technology, Harbin 150001, People's Republic of China*

(Received 8 September 2020; revised 1 August 2021; accepted 10 January 2022; published 26 January 2022)

Layered hybrid improper ferroelectrics are very important for multiferroic devices; however, it has been very challenging to obtain multiferroic properties at room temperature. In this study we report that acceptor-donor codoping can be used to realize ferromagnetism in $Ca_3Mn_2O_7$ improper ferroelectric ceramics at room temperature. The transmission electron microscope observation and first-principles calculation revealed that the obtained ferromagnetic properties result from the $MnO_6$ octahedron tilt caused by the large lattice distortion near the acceptor-donor pair. At the same time, an obvious magnetoimpedance effect was observed.

DOI: 10.1103/PhysRevB.105.014430

Multiferroic materials are expected to have widespread applications in storage, sensing, and microwave devices. Unfortunately, single-phase multiferroics are uncommon. Since theoretical calculations have predicted that layered improper ferroelectrics may have strong ferromagnetic-ferroelectric coupling effects at room temperature [1], improper ferroelectrics have attracted the interest of a diverse range of researchers [2]. The layered $A_{n+1}B_nO_{3n+1}$ perovskites with the Ruddlesden-Popper (RP) structure are typical improper ferroelectrics [3,4]. The ferroelectricity of RP improper ferroelectrics is thought to be caused by local structure changes by $BO_6$ octahedron tilts and rotations, and the antiferromagnetism is caused by the magnetic ions (such as $Mn^{4+}$) in octahedrons [5–8]. Because of the ferromagnetic-ferroelectric coupling effect achieved in a single phase, layered improper ferroelectrics have been considered viable candidates in multiferroic materials [9–11].

However, some disadvantages of RP improper ferroelectrics need to be overcome. On the one hand, the RP improper ferroelectrics have a very high barrier to ferroelectric polarization switching. Fennie *et al.* [12] demonstrated that the polarization switching barrier of $Ca_3Ti_2O_7$ is as high as 200 meV, which is higher than the $Ca_3Ti_2O_7$ breakdown electric field. Although the barriers are generally larger than those of traditional $ABO_3$ ferroelectrics, such as $BaTiO_3$ [13] and $PbTiO_3$ [14], the polarization switching barrier of $(Ca/Sr/Ba)_3(Sn/Zr/Ge)_2O_7$ can be reduced by composite doping. Liu *et al.* [15] used an ultraviolet-visible near-infrared spectrophotometer to test the energy gap of $Ca_3Mn_2O_7$. The energy gap of $Ca_3Mn_2O_7$ was 1.29 eV at room temperature. The energy gap of $Ca_3Mn_2O_7$ is very small, and it is difficult to obtain an electric hysteresis loop. On the other hand, low Néel temperature limits the applications of RP improper ferroelectrics. Because the Néel temperature of $Ca_3Mn_2O_7$ is about 115 K [16,17], it is challenging to design multiferroic properties in improper ferroelectrics at room temperature. Li *et al.* [18] found that structural distortion of $Ca_{2.94}Na_{0.06}Mn_2O_7$ reduces effectively compared with $Ca_3Mn_2O_7$, while orthogonal distortion and Jahn-Teller distortion reduced either. These two samples underwent an antiferromagnetic transition at 111 K, and the exchange bias and coercive field of $Ca_{2.94}Na_{0.06}Mn_2O_7$ increased. Zhang *et al.* [19] observed a quasi-two-dimensional antiferromagnetic fluctuation effect in $Li_{2x}Ca_{3-2x}Mn_2O_7$ ($x = 0$–$0.05$), and the antiferromagnetic order developed at 120 K.

Recently some studies have been conducted to investigate ways to lower the polarization switching barrier and improve the ferromagnetic properties of improper ferroelectrics, with a focus on strain design and doping engineering. The mismatch strain of epitaxial films was used to modify the properties of $ABO_3$ films [20]. Furthermore, it has been discovered that the strong correlation coupling of strain and a polarized lattice can result in the formation of a new stable ferroelectric phase in the nonpolar dielectric, increasing polarization and Curie temperature. Lu and Rondinelli [20] have demonstrated that biaxial strain induces a nonpolar-polar transition in a (001)-oriented $A_3B_2O$ film which is related to oxygen octahedral tilt and rotation. In addition, recent studies have shown that elemental doping is an effective method for improving improper ferroelectric properties. At room temperature, ferroelectric and ferroelastic domains exist in Sr-doped $(Ca, Sr)_3Ti_2O_7$ single crystals, according to Oh *et al.* [21]. The authors also stated that the ferroelectric domain switching is accomplished via an intermediate phase ($aa_0c_0$ tilting mode), resulting in a low coercive field [21]. Ma *et al.* [6] discovered that the dop-

*These authors contributed equally to this work.
†Corresponding authors: wld@hit.edu.cn
‡Corresponding authors: wdfei@hit.edu.cn

 

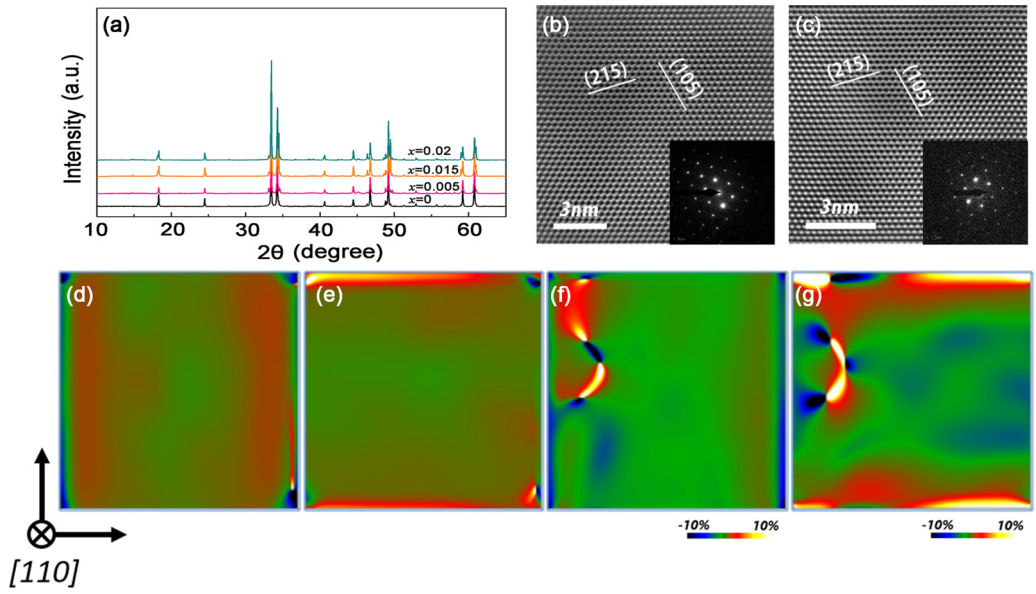


FIG. 1. XRD and TEM characterizations of $(Li_{0.5}Al_{0.5})_xCa_{3-x}Mn_2O_7$ ceramics. (a) The phase structure of $(Li_{0.5}Al_{0.5})_xCa_{3-x}Mn_2O_7$ ($x = 0, 0.005, 0.015, 0.02$) ceramics. (b) High-resolution phase of $Ca_3Mn_2O_7$ ceramic taken at room temperature. (c) High-resolution phase of $(Li_{0.5}Al_{0.5})_{0.005}Ca_{2.995}Mn_2O_7$ ceramic taken at room temperature. (d–e) Geometric phase analysis results of $Ca_3Mn_2O_7$ ceramic. (f–g) Geometric phase analysis results of $(Li_{0.5}Al_{0.5})_{0.005}Ca_{2.995}Mn_2O_7$ ceramic.

ing of the A site is essential in the $a_0a_0c_+$ tilting of RP layered crystals. Furthermore, the eccentricity of the $Mn^{4+}$ ion causes ferroelectricity in Pr-Sr codoped ferromagnetic $Ca_3Mn_2O_7$, which is stabilized by lattice distortion. Suitable codoping is beneficial to the tilting of $BO_6$ octahedron, as demonstrated by codoped $(Ca_ySr_{1-y})_{1.15}Tb_{1.85}Fe_2O_7$, which exhibits both polar and weak ferromagnetism at room temperature [22].

The formation of ionic pairs has been confirmed in some donor-acceptor codoped oxides, and the donor-acceptor pair leads to room-temperature ferroelectricity in $TiO_2$ ceramic binary oxide [23,24]. The great effects of the ionic pair on the phase transition and properties of $ABO_3$ ferroelectrics such as $BaTiO_3$ [23–26] and Pb(Zr, Ti)$O_3$ [27,28] ceramics have also been discovered.

Ionic pairs were introduced into $Ca_3Mn_2O_7$ in this study via acceptor-donor codoping. At room temperature, weak ferromagnetism and an enhanced magnetoimpedance effect were observed in $Li^+ - Al^{3+}$ codoped $Ca_3Mn_2O_7$ ceramics. Our results suggest that ionic pair doping could be used to design room-temperature $Ca_3Mn_2O_7$ improper ferroelectrics.

The sol-gel method was used to synthesize $(Li_{0.5}Al_{0.5})_xCa_{3-x}Mn_2O_7$. $Ca(NO_3)_2 \cdot 4H_2O$, $Mn(NO_3)_2$, $C_9H_{21}AlO_3$, $CH_3COOLi \cdot 2H_2O$, and citric acid were mixed uniformity in glycol. After being burned and compressed into pellets, the powder was ball milled, then sintered at 1350 °C for 48 hours. X-ray powder diffraction (XRD, PANalytical Empyren) with Cu $K$ a radiation was used to characterized samples. The transmission electron microscope (TEM, FEI Tecnai G2 F20) was used to examine the samples' microstructures. The x-ray photoelectron spectrometer (XPS, ESALAB 250Xi) was used to characterize the element valence. The dielectric properties of ceramic samples under varying magnetic field strengths were tested using a vibrating sample magnetometer (IDAW-2000D) and an Agilent 4294 A impedance analyzer. The samples were tested for hysteresis loops using a Lakeshore 7407 VSM manufactured in the

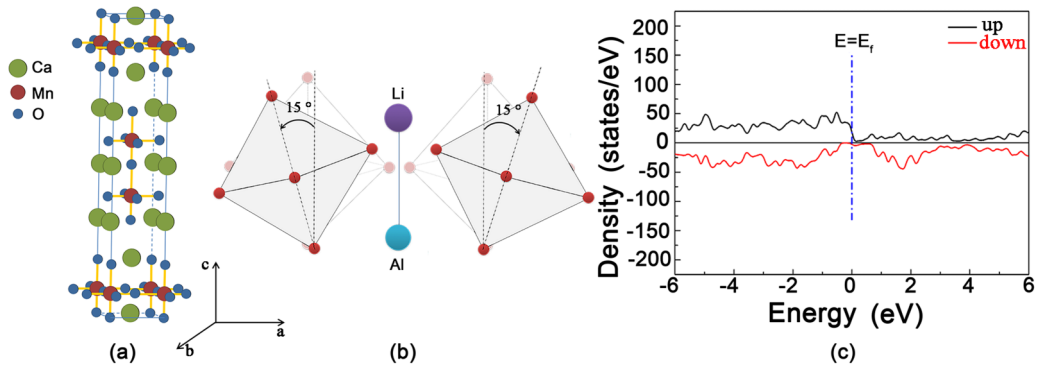


FIG. 2. Calculation results of $(Li_{0.5}Al_{0.5})_xCa_{3-x}Mn_2O_7$ based on first principles. (a) Schematic diagram of $Ca_3Mn_2O_7$ crystal structure. (b) $MnO_6$ octahedron tilt deviates from the iron pair direction. (c) Density of states calculation result of $Ca_3Mn_2O_7$ after doping.

TABLE I. The first-principles calculation results of four kinds of "$Li^+$–$Al^{3+}$" occupy states.

| | Occupy state 1 | Occupy state 2 | Occupy state 3 | Occupy state 4 |
|---|---|---|---|---|
| The $MnO_6$ angle of tilting | 15.512 ° | 12.552 ° | 15.514 ° | 9.169 ° |
| Ferromagnetism | Yes | Yes | Yes | Yes |

United States. The magnetization-temperature curve tests on samples were performed using the high-precision magnetic measuring instrument MPMS, which is based on semiconductor quantum interference design (SQUID) detection technology and is manufactured in the United States by Quantum Design.

Figure 1(a) shows the XRD patterns of $(Li_{0.5}Al_{0.5})_xCa_{3-x}Mn_2O_7$ ceramics with various $x$ values, and all samples were found to be a single phase with the crystal structure of improper ferroelectric $Ca_3Mn_2O$. In addition, scanning electron microscopy (SEM) images (Supplemental Material [29]) revealed homogenous needlelike microstructure. High-resolution TEM (HRTEM) images of $Ca_3Mn_2O_7$ and $(Li_{0.5}Al_{0.5})_{0.005}Ca_{2.995}Mn_2O_7$ ceramics are shown in Figs. 1(b) and 1(c), respectively, and the corresponding fast Fourier transformation diffractogram is shown in the insert figures. Both the HRTEM images and the diffraction patterns indicate that the crystal structure of codoped $(Li_{0.5}Al_{0.5})_{0.005}Ca_{2.995}Mn_2O_7$ ceramics is the same as that of pure $Ca_3Mn_2O_7$, which is consistent with other studies [18,19].

The lattice strain was obtained by geometric phase analysis (GPA) of HRTEM images. The normal strain distributions of $\varepsilon_{xx}$ and $\varepsilon_{yy}$ of pure $Ca_3Mn_2O_7$ ceramics are shown in Figs. 1(d) and 1(e), and the uniform contrast shown in the GPA color charts indicates that there is no noticeable lattice distortion or strain in the pure $Ca_3Mn_2O_7$ sample. However, large local strain can be clearly observed in the GPA color charts of both $\varepsilon_{xx}$ and $\varepsilon_{yy}$ for the $(Li_{0.5}Al_{0.5})_{0.005}Ca_{2.995}Mn_2O_7$ sample, as shown in Figs. 1(f) and 1(g). Furthermore, the doped ceramic's local stress appears as a tensile stress-compressive stress pair. Generally, there is a Coulomb force between "$Li^+$–$Al^{3+}$," which causes the two ions to gravitate toward each other. The bonding force causes $Li^+$ and $Al^{3+}$ to vibrate near their respective lattice sites at the same time. The combined action of these two forces will cause "$Li^+$–$Al^{3+}$" to appear in adjacent lattice sites. Simultaneously, based on the transmission electron microscope stress simulation results, it is known that the doped "$Li^+$–$Al^{3+}$" exists in the form of ion pairs in $Ca_3Mn_2O_7$ ceramics. We believe that the large local strain is caused by $Li^+$–$Al^{3+}$ ionic pairs because no crystal defects, such as dislocation, stacking faults, or twin, were observed during HRTEM observation of the $(Li_{0.5}Al_{0.5})_{0.005}Ca_{2.995}Mn_2O_7$ sample. Ionic pair-induced local strains have also been observed in ionic pair-doped $TiO_2$ [30] and $BaTiO_3$ ceramics [23,24,31].

To investigate the effects of $Li^+$–$Al^{3+}$ ionic pairs on the atomic and electronic structures of $Ca_3Mn_2O_7$, first-

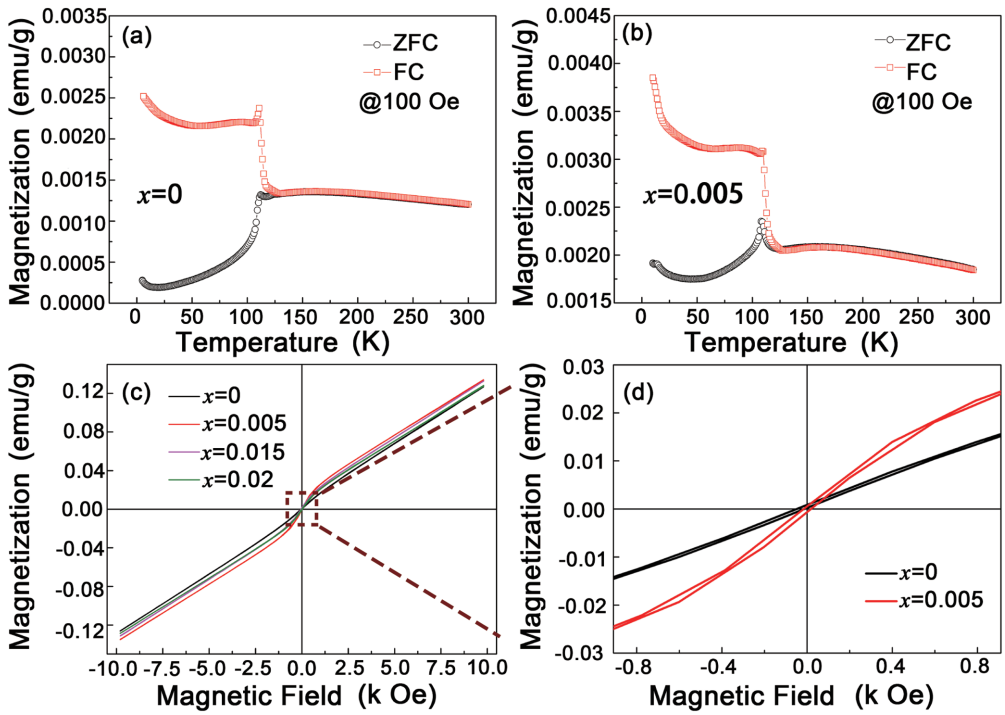


FIG. 3. Magnetic performance characterization of $(Li_{0.5}Al_{0.5})_{0.005}Ca_{2.995}Mn_2O_7$. (a, b) Zero-field-cooled and field-cooled curves of $(Li_{0.5}Al_{0.5})_xCa_{3-x}Mn_2O_7$ ($x = 0, 0.005$) ceramics under 100 Oe. (c, d) Hysteresis loop of $(Li_{0.5}Al_{0.5})_xCa_{3-x}Mn_2O_7$ ($x = 0, 0.005, 0.015, 0.02$) ceramics at room temperature and local amplification of hysteresis loop under low magnetic field of $(Li_{0.5}Al_{0.5})_xCa_{3-x}Mn_2O_7$ ($x = 0, 0.005$).

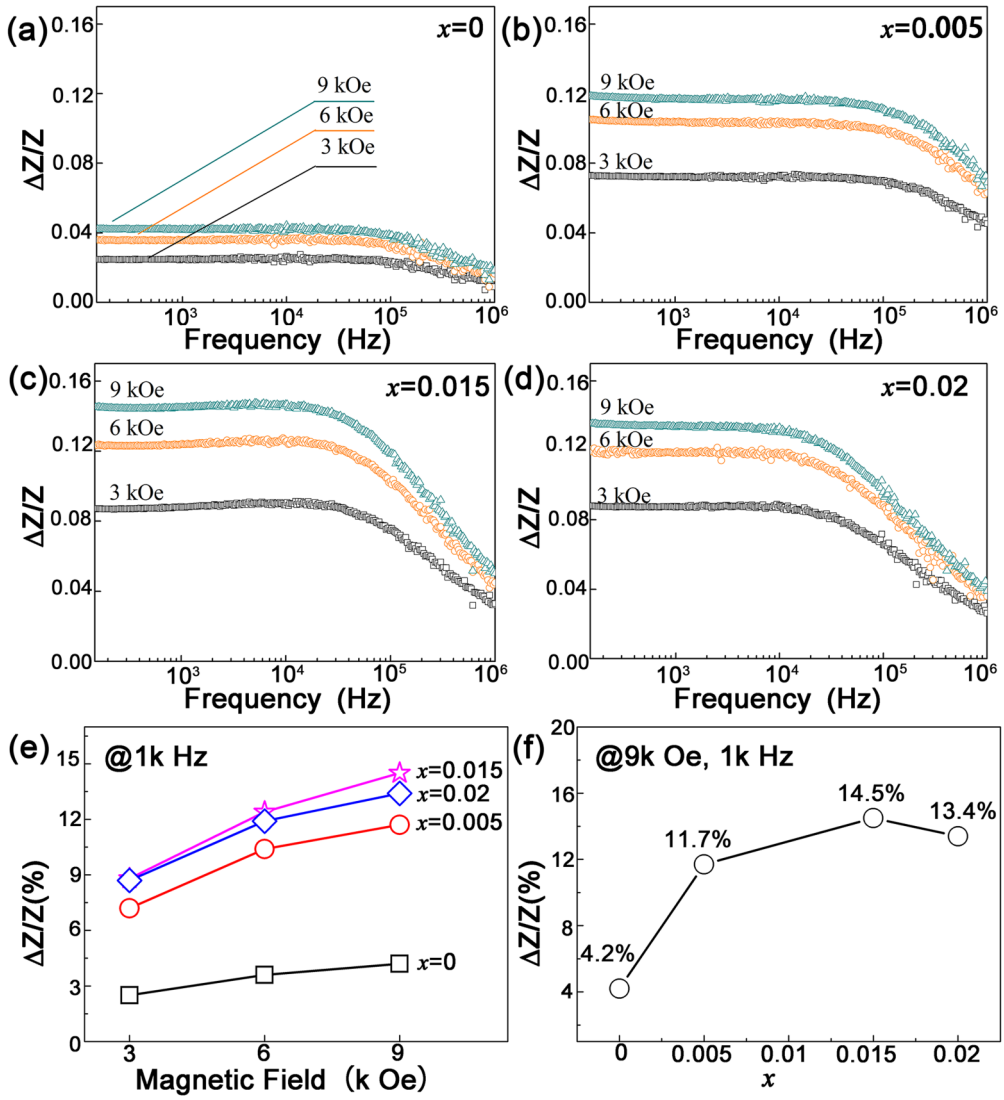


FIG. 4. Variation rules of magnetoresistance change rate with frequency under different magnetic field strengths. (a–d) Magnetoresistance behaviors change with frequency of $(Li_{0.5}Al_{0.5})_xCa_{3-x}Mn_2O_7$ ($x = 0, 0.005, 0.015, 0.02$). (e) Magnetoresistance change rate of $(Li_{0.5}Al_{0.5})_xCa_{3-x}Mn_2O_7$ ($x = 0, 0.005, 0.015, 0.02$) under 3 kOe, 6 kOe, and 9 kOe. (f) Magnetoresistance change rate of $(Li_{0.5}Al_{0.5})_xCa_{3-x}Mn_2O_7$ change with doping content under 9 kOe at1 kHz.

principles calculation based on density functional theory (DFT) were performed. Four different kinds of occupy states have been calculated by the Vienna Ab-initio Simulation Package (VASP), in which $Li^+$ and $Al^{3+}$ occupy neighbors along the *c* axis, the diagonal of the face or body in the perovskite layer, and separated by $Ca^{2+}$ [29]. According to the calculation, the band gap of different occupied states of codoped $Ca_3Mn_2O_7$ are approximately 200 meV, which is similar to the band of pure $Ca_3Mn_2O_7$ [12]. The calculation also confirms that a large lattice distortion is induced around the "$Li^+$–$Al^{3+}$" ionic pair. Several different "$Li^+$–$Al^{3+}$" occupancy states possibly existed, but their calculation shows that the different occupancy states of the $MnO_6$ octahedrons would all tilt with slightly different angles. The angle of tilting of $MnO_6$ octahedron for these four occupancy states is 15.512°, 12.552°, 15.514°, and 9.169°, respectively. A schematic diagram of the $MnO_6$ octahedron tilt is shown in Figs. 2(a) and 2(b), when "$Li^+$–$Al^{3+}$" are nearest neighbors in their sublattices. DFT calculations for four kinds of "$Li^+$–$Al^{3+}$" occupying states of $Ca_3Mn_2O_7$ indicate that the total number of spin-up electron states differs slightly from that of spin-down electron states, which may cause weak ferromagnetism in "$Li^+$–$Al^{3+}$" codoped ceramics [29]. The specific four occupying states of the $MnO_6$ octahedron tilt angle and density of states are shown in Table I.

The magnetic properties of $Ca_3Mn_2O_7$ and $(Li_{0.5}Al_{0.5})_{0.005}Ca_{2.995}Mn_2O_7$ ceramics are illustrated in Fig. 3. The magnetization-temperature curves shown in Figs. 3(a) and 3(b) show that the doping element has no effect on the Néel temperature (about 115 K) of the ceramics, even when the doping concentration is increased to 2% (as shown in Fig. S4 [29]). However, magnetic hysteresis loop measurements show that the $Li^+$–$Al^{3+}$ codoped $(Li_{0.5}Al_{0.5})_{0.005}Ca_{2.995}Mn_2O_7$ ceramic exhibits weak ferromagnetism at room temperature when compared to

the pure $Ca_3Mn_2O$ sample. The weak ferromagnetism may be caused by local lattice distortion around the $Li^+$–$Al^{3+}$ pair, which agrees with the DFT calculations. Because ferromagnetism exists only in the region near the ionic pair, the ferroelectric properties observed in the codoped ceramics are very weak. Previous studies [18,19] demonstrated that ferromagnetic properties could be observed in strained improper ferroelectrics. In this work the strain is induced by the ionic pair. Because the lattices far from the ionic pair are almost strain-free and exhibit the same antiferromagnetic transition behavior as pure $Ca_3Mn_2O_7$ crystal, the apparent Néel temperature of $(Li_{0.5}Al_{0.5})_xCa_{3-x}Mn_2O_7$ ceramic remains unchanged when compared to pure $Ca_3Mn_2O_7$ ceramic.

The relations between the magnetoimpedance effect (MIE) and frequency, measured at various magnetic fields for $(Li_{0.5}Al_{0.5})_xCa_{3-x}Mn_2O_7$ ceramics, are shown in Fig. 4. MIEs have been discovered in all ceramics, but the MIE of pure $Ca_3Mn_2O_7$ ceramic is much smaller than those of $(Li_{0.5}Al_{0.5})_xCa_{3-x}Mn_2O_7$ ceramics, as shown in Figs. 4(a)–4(d). Figure 4(e) shows the effect of a magnetic field on the MIE of ceramics at 1 kHz. MIEs of ceramics increase with the magnetic field, but the increasing rates of codoping ceramics are more significant than that of pure $Ca_3Mn_2O_7$ ceramic. The MIE can be improved by $Li^+$–$Al^{3+}$ codoping, as shown in Fig. 4(f). The MIE increased to 11.7% at the magnetic field of 9 kOe when the codoping content was 0.5%. Moreover, at a codoping content of 1.5%, the MIE of codoping ceramic reaches a maximum value of 14.5%. When the codoping is increased further, MIE decreases in proportion to the codoping content.

A previous study [30] found that the electric dipolar of an ionic pair polarizes the region around the pair, resulting in ferroelectric and piezoelectric responses in $TiO_2$ binary oxide. In the case of $Li^+$–$Al^{3+}$ codoped $Ca_3Mn_2O_7$, the oxygen octahedral tilt and rotation are induced as given in the DFT calculation, which can lead to local ferroelectricity according to previous studies [12]. Meanwhile, the region near the ionic pair is highly strained and ferromagnetic, and local multiferroic regions induce MIE in high magnetic fields. Magnetostriction is thought to cause the polarization in the region near the ionic pair, and polarization generates an electric field which effectively scatts carriers and enhances the impedance of codoping ceramics.

In this stud, we demonstrated room-temperature ferromagnetism and MIE in $Li^+$–$Al^{3+}$ codoped $Ca_3Mn_2O_7$ ceramics. Both TEM observation and DFT calculation show that the $Li^+$–$Al^{3+}$ pair causes significant local lattice distortion in the vicinity of the pair, and the DFT calculation also indicates that the $MnO_6$ octahedrons near the $Li^+$–$Al^{3+}$ pair tilt with large angles. The strained region near the ionic pair is thought to generate ferromagnetism and MIE. The current study demonstrates a simple and effective method for modifying the properties of $Ca_3Mn_2O_7$ improper ferroelectrics.

This work was supported by the National Natural Science Foundation of China (No. 51802056), the Science Foundation of the National Key Laboratory of Science and Technology on Advanced Composites in Special Environments, and the Key Laboratory of Micro-systems and Micro-structures Manufacturing (Harbin Institute of Technology), Ministry of Education.

[1] S. F. Matar, V. Eyert, A. Villesuzanne, and M. H. Whangbo, Phys. Rev. B **76**, 054403 (2007).
[2] Y. Zhang, J. Wang, and P. Ghosez, Phys. Rev. Lett. **125**, 157601 (2020).
[3] S. N. Ruddlesden and P. Popper, Acta Crystallogr. **10**, 538 (1957).
[4] S. Ruddlesden and P. Popper, Acta Crystallogr. **11** 54 (1958).
[5] S. Picozzi, K. Yamauchi, B. Sanyal, I. A. Sergienko, and E. Dagotto, Phys. Rev. Lett. **99**, 227201 (2007).
[6] C. Ma, Y. Lin, H. X. Yang, H. F. Tian, L. Shi, J. Zeng, and J. Q. Li, Adv. Mater. **27**, 6328 (2015).
[7] A. Glamazda, D. Wulferding, P. Lemmens, B. Gao, S. W. Cheong, and K. Y. Choi, Phys. Rev. B **97**, 094104 (2018).
[8] F. Ye, J. Wang, J. Sheng, C. Hoffmann, T. Gu, H. J. Xiang, W. Tian, J. J. Molaison, A. M. dos Santos, M. Matsuda, B. C. Chakoumakos, J. A. Fernandez-Baca, X. Tong, B. Gao, J. W. Kim, and S. W. Cheong, Phys. Rev. B **97**, 041112(R) (2018).
[9] P. Rocha-Rodrigues, S. S. M. Santos, I. P. Miranda, G. N. P. Oliveira, J. G. Correia, L. V. C. Assali, H. M. Petrilli, J. P. Araújo, and A. M. L. Lopes, Phys. Rev. B **101**, 064103 (2020).
[10] M. S. Senn, A. Bombardi, C. A. Murray, C. Vecchini, A. Scherillo, X. Luo, and S. W. Cheong, Phys. Rev. Lett. **114**, 035701 (2015).
[11] A. B. Harris, Phys. Rev. B **84**, 064116 (2011).
[12] N. A. Benedek and C. J. Fennie, Phys. Rev. Lett. **106**, 107204 (2011).
[13] R. E. Cohen and H. Krakauer, Phys. Rev. B **42**, 6416 (1990).
[14] U. V. Waghmare and K. M. Rabe, Phys. Rev. B **55**, 6161 (1997).
[15] M. F. Liu, Y. Zhang, L. F. Lin, L. Lin, S. W. Yang, X. Li, Y. Wang, S. Z. Li, Z. B. Yan, X. Z. Wang, X. G. Li, S. Dong, and J. M. Liu, Appl. Phys. Lett. **113**, 022902 (2018).
[16] W. Zhu, L. Pi, Y. Huang, S. Tan, and Y. Zhang, Appl. Phys. Lett. **101**, 192407 (2012).
[17] M. V. Lobanov, M. Greenblatt, E. N. Caspi, J. D. Jorgensen, D. V. Sheptyakov, B. H. Toby, C. E. Botez, and P. W. Stephens, J. Phys.: Condens. Matter **16**, 5339 (2004).
[18] S. Y. Li, S. Y. Wang, Y. G. Lu, C. Zhang, X. X. Yang, J. Gao, D. J. Li, Y. Zhu, and W. F. Liu, AIP Adv. **8**, 015009 (2018).
[19] X. N. Zhang, W. F. Liu, Y. L. Han, C. Huang, P. Wu, W. Zhou, J. Gao, G. H. Rao, and S. Y. Wang, J. Mater. Chem. C **5**, 7011 (2017).
[20] X. Z. Lu and J. M. Rondinelli, Nat. Mater. **15**, 951 (2016).
[21] Y. S. Oh, X. Luo, F. T. Huang, Y. Wang, and S. W. Cheong, Nat. Mater. **14**, 407 (2015).
[22] M. J. Pitcher, P. Mandal, M. S. Dyer, J. Alaria, P. Borisov, H. Niu, J. B. Claridge, and M. J. Rosseinsky, Science **347**, 420 (2015).
[23] Y. Feng, W. L. Li, D. Xu, Y. L. Qiao, Y. Yu, Y. Zhao, and W. D. Fei, ACS Appl. Mater. Interfaces **8**, 9231 (2016).
[24] D. Xu, W. L. Li, L. D. Wang, W. Wang, W. P. Cao, and W. D. Fei, Acta Mater. **79**, 84 (2014).

[25] D. Xu, W. L. Li, L. D. Wang, W. Wang, and W. D. Fei,, RSC Adv. **4**, 34008 (2014).

[26] D. Xu, L. D. Wang, W. L. Li, W. Wang, Y. F. Hou, W. P. Cao, Y. Feng, and W. D. Fei, Phys. Chem. Chem. Phys. **16**, 13078 (2014).

[27] Y. Feng, W. L. Li, D. Xu, W. P. Cao, Y. Yu, and W. D. Fei, RSC Adv. **6**, 36118 (2016).

[28] Y. Feng, W. L. Li, Y. Yu, H. N. Jia, Y. L. Qiao, and W. D. Fei, Phys. Rev. Mater. **1**, 064405 (2017).

[29] See Supplemental Material at http://link.aps.org/supplemental/10.1103/PhysRevB.105.014430 for microstructure, density functional theory, magnetic properties, and x-ray photoelectron spectrometer results of $(Li_{0.5}Al_{0.5})xCa_{3-x}Mn_2O_7$ ceramics.

[30] Y. Yu, L. D. Wang, W. L. Li, Y. L. Qiao, Y. Zhao, Y. Feng, T. D. Zhang, R. X. Song, and W. D. Fei, Acta Mater. **150**, 173 (2018).

[31] Y. Huang, C. Zhao, J. Yin, X. Lv, J. Ma, and J. Wu, J. Mater. Chem. A **7**, 17366 (2019).